Phys Chem Minerals (2004) 31: 92–101
DOI 10.1007/s00269-003-0371-x

ORIGINAL PAPER

C. Viti · G. Di Vincenzo · M. Mellini

Thermal transformations in laser-heated chloritized annite

Received: 6 January 2003 / Accepted: 14 October 2003

Abstract Chloritized annite from the Irizar granite has been used for laser-heating experiments, following the procedures used for ^{40}Ar–^{39}Ar dating (heating steps in the 600–1080 °C temperature range). Four runs, at different temperatures, have been characterized using transmission electron microscopy, electron diffraction, micro-Raman and micro-IR spectroscopies. The water loss was evaluated by thermogravimetry. The chlorite domains break down first forming (001) amorphous layers, that later coalesce to rounded, equant inclusions and finally recrystallize to olivine and spinels plus silica glass. These phases occur within negative crystals hosted in ordered dehydrated annite, produced by dehydration and annealing of the starting annite. Dehydrated annite, olivine and spinels display topotactic relationships, determined by the common orientation of closely packed oxygen layers.

Keywords Laser heating · Chloritized annite · Dehydration · Negative crystals · Topotactic reactions

Introduction

Laser heating and laser ablation are common experimental techniques. In analytical geochemistry, laser energy is used to vaporize the specimen in several determinations, such as ICP-LA-MS (inductively coupled plasma- laser ablation- mass spectroscopy) or ^{40}Ar–^{39}Ar laser-probe dating, with laser beam designed to produce a localized, destructive effect on the specimen. Experimental mineralogy may adopt a softer approach; for instance, HP–HT experiments are often carried out on tiny crystals within pressurized diamond-anvil cells, measuring pressure and increasing temperature through laser pulses. In the latter case, a common assumption is that the physical state of the specimen is not altered during the experiment.

During a previous ^{40}Ar –^{39}Ar laser probe and transmission electron microscopy (TEM) investigation of chloritized biotites (Di Vincenzo et al. 2003), we became interested in understanding the chemical and structural modifications induced by laser heating. The original aim was to explain the hump-shaped age profiles (with meaningless young and old age steps) from chloritized biotites. However, that study also revealed fast laser-induced transformations, occurring in both chlorite and biotite. In particular, close to 600 °C, chlorite and biotite underwent deformation and bending. Heated at 800 °C, chlorite disappeared, while biotite recrystallized together with new phases formed by chlorite breakdown. These new phases occurred within euhedral negative crystals, hosted within highly ordered, recrystallized mica.

In this paper, we discuss the chemical, textural and structural details of these transformations.

C. Viti (✉) · M. Mellini
Dipartimento di Scienze della Terra,
Università di Siena Via Laterina,
8, 53100 Siena, Italy
Tel.: +39 577 233830
Fax: +39 577 233938
e-mail: vitic@unisi.it

G. Di Vincenzo
Istituto di Geoscienze e Georisorse – CNR Via Moruzzi,
1, 56124 Pisa, Italy

Specimen description and experimental details

The specimen (no. AR8) comes from a granitic dyke which intrudes the Irizar granite in northern Victoria Land, Antarctica (Di Vincenzo et al. 2003). Petrographic observations and X-ray diffraction data indicate chloritization of biotite, with d_{001} of 10.133 and 14.293 Å for biotite and chlorite, respectively. The amount of chlorite (43%) was determined by intensities of basal reflections, using the $(002)_{chl}/[(002)_{chl} + (001)_{bt}]$ ratio, as proposed by Maniar and Cooke (1997).

Chemical compositions (electron microprobe analyses) correspond to annite and chamosite, with cation contents $K_{0.90}$ $(Mg_{0.75}$ $Fe_{1.82}$ $Ti_{0.25}$ $Mn_{0.04}$ $Al_{0.23})$ $(Si_{2.88}$ $Al_{1.12})$ and $(Mg_{1.14}$ $Fe_{3.26}$ $Mn_{0.13}$ $Al_{1.40})$ $(Si_{2.73}$ $Al_{1.27})$, respectively. Annite and chamosite obviously

Table 1 Sequences of laser-heating steps in the 0.3-, 0.7-, 1.2- and 2.2-W experiments. Estimated temperatures (°C) are shown *in parentheses*

Heating step	Sample 0.3 W (600 °C)	Sample 0.7 W (810 °C)	Sample 1.2 W (940 °C)	Sample 2.2 W (1080 °C)
1	0.15 (485)	0.35 (640)	0.35 (640)	0.35 (640)
2	0.30 (600)	0.47 (710)	0.51 (730)	0.51 (730)
3	–	0.60 (760)	0.70 (810)	0.80 (840)
4	–	0.70 (810)	1.00 (890)	1.10 (910)
5	–	–	1.20 (940)	1.50 (990)
6	–	–	–	2.20 (1080)

differ in potassium and aluminum contents; moreover, chamosite is Fe- and Mn-enriched and Ti-depleted with respect to annite.

Specimens for laser heating and TEM investigation were selected from biotite separates (flakes > 0.5 mm in diameter). Heating experiments were performed step by step under ultrahigh vacuum (UHV), using a multimode CW Nd-YAG infrared laser ($\lambda = 1064$ nm). Four experiments were carried out, up to 0.3, 0.7, 1.2 and 2.2 W, respectively (Table 1). Each heating step lasted 2 min and was followed by 3 min of evacuation. Temperatures were estimated by an optical pyrometer, whereas temperature homogeneity through the sample was verified by a thermal CCD camera.

Untreated and laser-heated samples were glued onto TEM copper grids with the *c* axis parallel to the grid. They were carefully prethinned using emery paper, in order to reach ~30 μm thickness. Later, they were thinned by Ar^+ ion milling, using a Gatan Dual Ion Mill (5 kV and 20 ° in the first step; 1.5 kV and 12 ° in the final thinning step).

TEM was carried out using a Jeol 2010, working at 200 kV and equipped with an ultra-high-resolution (UHR) pole piece, capable of point-to-point resolution close to 1.9 Å. The microscope is equipped with a semi-STEM system and an ultrathin window energy-dispersive spectrometer (EDS–ISIS Oxford). The electron probe can be focused to a 50-Å spot. EDS data were treated according to the procedures given in Cliff and Lorimer (1975) and in Mellini and Menichini (1985). SAED patterns were calibrated against the d_{001} spacing of untreated annite ($d_{001} = 10.13$ Å), measured by X-ray powder diffraction (XRPD). Electron images have been recorded by either normal photographic films or imaging plates (Fuji film FDL5000).

Annite crystals in thin sections or ion-thinned flakes were also investigated by micro-IR and micro-Raman spectroscopies. IR spectra were collected by a Nicolet Magna–IR 560 spectrometer equipped with globar source, MCT/A detector, Ge-KBr beamsplitter and coupled with a NicPlan infrared microscope; spot size ranges from 10 to 30 μm. Raman spectra were obtained using a Labram microspectrometer. The excitation source was an Ar^+ ion laser, operating at 514.5 nm wavelength and 100 mW power. In both micro-IR and micro-Raman experiments, best results (in terms of peak/background ratio and minimal fluorescence) were obtained using ion-thinned grids (thus sampling small volumes).

Thermal analyses (thermogravimetry, TG, and differential thermogravimetry, DTG) were carried out using a Seiko SSC 5200 thermal analyzer in the 25–1200 °C temperature range, with 20 °C min^{-1} heating rate, under 100 ml min^{-1} He flux. The thermal analyzer was equipped with a mass spectrometer ESS GeneSys Quadstar 422, used to identify the gases released during heating. Two samples (no. AR8 and, for comparison, no. A13, a nearly chlorite-free annite described in Di Vincenzo et al. 2003) were prepared by wet-grinding annite separates. The amounts of powder used for thermal analyses were 13.01 and 13.99 mg, for samples AR8 and A13, respectively.

Results

TEM observations

Untreated annite

Annite is finely associated to chamosite, in agreement with optical and XRPD data (Di Vincenzo et al. 2003). Annite to chamosite alteration mostly occurs at the cleavage planes, with chlorite intergrown to mica down to the unit-cell scale. Otherwise, it forms large domains, consisting of ordered 14-Å sequences, up to 200–500 Å thick.

Figure 1a shows the [010] electron diffraction pattern of untreated annite, indicating 1*M* polytype. The d_{001}

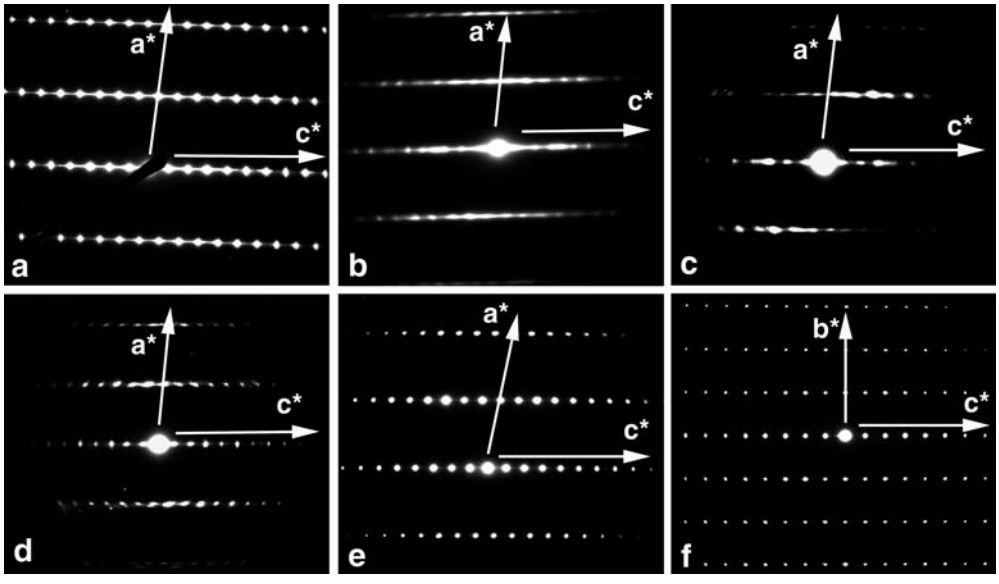

Fig. 1a–f [010] SAED patterns of **a** untreated sample; **b** 0.3-W sample (600 °C); **c** 0.7-W sample (810 °C); **d** 1.2-W sample (940 °C); **e** 2.2-W sample (1080 °C). **f** [100] SAED pattern of 2.2-W sample (1080 °C)

and d_{100} spacings are 10.13 and 5.34 Å, respectively ($c =$ 10.29 Å and $a = 5.42$ Å). No [100] pattern was collected. Diffuse streaking commonly occurs along c^*, due to disordered mica–chlorite interlayering.

TEM-EDS compositions of annite and chamosite are shown in Table 2.

Sample heated at 0.3 W (~600 °C)

The 0.3-W specimen is compact and similar to the untreated one. However, SAED patterns (Fig 1b) suggest decreasing crystallinity, with weaker and more diffuse diffraction effects. Streaking along c^* is present. Chlorite and mica layers are disturbed; the layers are often bent, with frequent interlayer parting; moreover, the chlorite layers are affected by incipient amorphization, suggested by vanishing 14 Å fringes. In contrast, annite is still present, even though with decreased crystallinity. No other phase was detected.

Sample heated at 0.7 W (~810 °C)

The most important textural feature of the 0.7-W sample is delamination, roughly parallel to the cleavage plane, producing packets 100–1000 Å thick. Each packet is delimitated by a thin amorphous layer, produced during laser heating. Laser-induced amorphization preferentially occurs at the cleavage plane within the most altered regions, characterized by abundant chlorite.

SAED patterns (Fig. 1c) reveal poorly crystalline samples. Reflections are weak and diffuse, but streaking along c^* is less evident than in the 0.3-W sample, possibly due to chlorite disappearance.

High-resolution images show incipient crystallization of the chlorite breakdown products (spinels and olivines plus amorphous silica, as described below in the 2.2 W section).

Table 2 TEM-EDS data (apfu) for the untreated sample (*ann* annite; *cham* chamosite) and for the 2.2-W sample (*dehyann* dehydrated annite; *Al-spl*, *Fe-spl* spinels, olivine and silica glass)

Untreated	K	Mg	Fe	Ti	Mn	Al	Si
ann	0.87	0.73	1.82	0.27	0.06	1.36	2.89
cham	0.00	1.13	3.25	0.06	0.07	2.23	3.25
2.2 W	K	Mg	Fe	Ti	Mn	Al	Si
dehyann	0.89	0.77	1.69	0.24	0.03	1.42	2.96
Al-spl	0.00	0.19	0.82	0.03	0.00	1.96	0.00
Fe-spl	0.00	0.17	2.24	0.16	0.00	0.43	0.00
olivine	0.00	0.77	1.01	0.00	0.05	0.00	1.00
glass	0.00	0.00	0.07	0.00	0.00	0.25	0.68

Sample heated at 1.2 W (~940 °C)

The 1.2-W sample displays major differences with respect to the 0.7-W sample: (1) although still present, delamination now occurs less frequently; (2) mica is more crystalline. Mica SAED patterns (Fig. 1d) show intense, sharp reflections, with 10-Å periodicity. Streaking along c^* is limited.

The mica (001) lattice fringes form regular sequences, up to 150–200 Å thick. Lattice fringes do not exhibit deformation, bending, dislocation and other defects. As in the previous sample, mica coexists with chlorite decomposition products. The new phases (olivine and spinels) occur as crystallites, up to 200 Å in size, typically elongated parallel to mica (001).

Sample heated at 2.2 W (~1080 °C)

Overall texture. Figure 2a shows the final texture obtained after heat treatment up to 1080 °C. The complex texture consists of ordered mica (light contrast matrix) that includes different new phases (dark grains). These have variable size (up to 2000 Å), shape, crystallinity, composition and crystallographic relations with respect to the host mica. Delamination is completely absent.

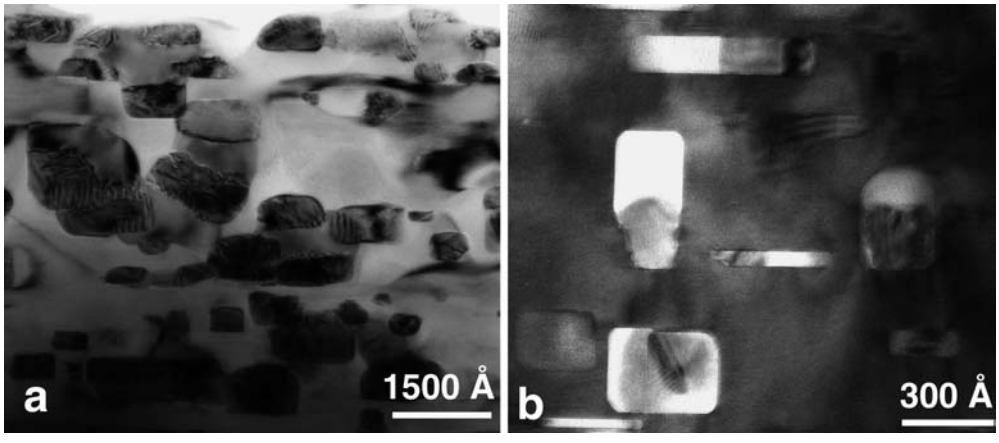

Fig. 2 a Typical texture of the 2.2-W (1080 °C) sample, with ordered mica (*light matrix*) hosting the chlorite breakdown products (*dark grains*). **b** Euhedral negative crystals in mica, hosting the chlorite breakdown products. In both images, mica [001] is *vertical*

We note the frequent occurrence of negative crystals, i.e., almost euhedral inclusions having habit and orientation imposed by the host mineral symmetry (Viti and Frezzotti 2001). Negative crystals are hosted within mica and display variable size and habit, from equant to elongated (Fig. 2b). They include chlorite breakdown products, namely crystalline spinels and olivine (dark contrast) plus amorphous material (silica glass, with light contrast).

Dehydrated annite. As spectroscopic and thermal analyses indicate that mica becomes completely anhydrous after heating, we will refer to it as dehydrated annite.

Due to thermal annealing, the dehydrated annite SAED patterns reveal crystallinity higher than in the previous samples (Fig. 1e, f). Diffraction spots are intense and sharp, streaking along c^* is absent. Measured interplanar spacings are $d_{001} = 10.09$ Å ($c = 10.25$ Å, compared to 10.29 in untreated annite), $d_{100} = 5.35$ Å ($a = 5.43$ Å, compared to 5.42 in untreated annite) and $d_{010} = 9.33$ Å.

The polytypic sequence ($1M$) is unchanged with respect to untreated annite. However, we now observe the occurrence in the same flake (expected to be one single crystal with defined crystal orientation) of different regions alternatively producing the [010] or [100] diffraction patterns (Fig. 1e and f, respectively). We interpret this feature as due to the occurrence of two orientation variants resulting from thermal breakdown and recrystallization. Whereas the [001] direction is conserved over the whole crystal, from point to point the pseudohexagonal mica layer reduces its symmetry inverting the [100] and [010] directions. Namely, the hexagonally close-packed oxygen layers of mica are conserved through the thermal transformation, with inversion of the a and b directions.

Dehydrated annite is highly ordered. (001) lattice fringes form thick regular sequences, with no defects, layer bendings or interlayering with other layer silicates. Dislocations and bent layers may locally occur close to inclusions and negative crystals.

TEM-EDS analyses of dehydrated annite (Table 2) are similar to the untreated sample, thus indicating that the thermal transformation (i.e. dehydration plus annealing) did not produce significant cation partitioning (apart from iron, apparently decreasing from 1.82 apfu in the untreated sample to 1.69 in the 2.2-W sample).

The chlorite breakdown products. Despite nanochemical and nanotextural variability, three main products were distinguished: 1) spinels, 2) olivine and 3) glass.

1. Spinels (Spl) occur as crystalline, large grains (up to 1000 Å, typically close to 500 Å), with dark contrast with respect to host-dehydrated annite.

Dehydrated annite and spinel share strongly related topotactic orientations (Fig. 3). The inset of Fig. 3 shows overlapped $[0\bar{1}1]_{spl}$ and $[010]_{dehyann}$ SAED patterns, with $[111]^*_{spl}$ parallel to $c^*_{dehyann}$. This orientation is unequivocally determined on the basis of the observed interplanar spacings of spinel, close to 8.35 and 3.00 Å for d_{100} and d_{022}, respectively.

The two lattices do not exactly coincide, due to minor differences in the interplanar spacings (e.g. d_{002} of dehydrated annite is close to 5 Å, whereas d_{111} of spinel is close to 4.8 Å).

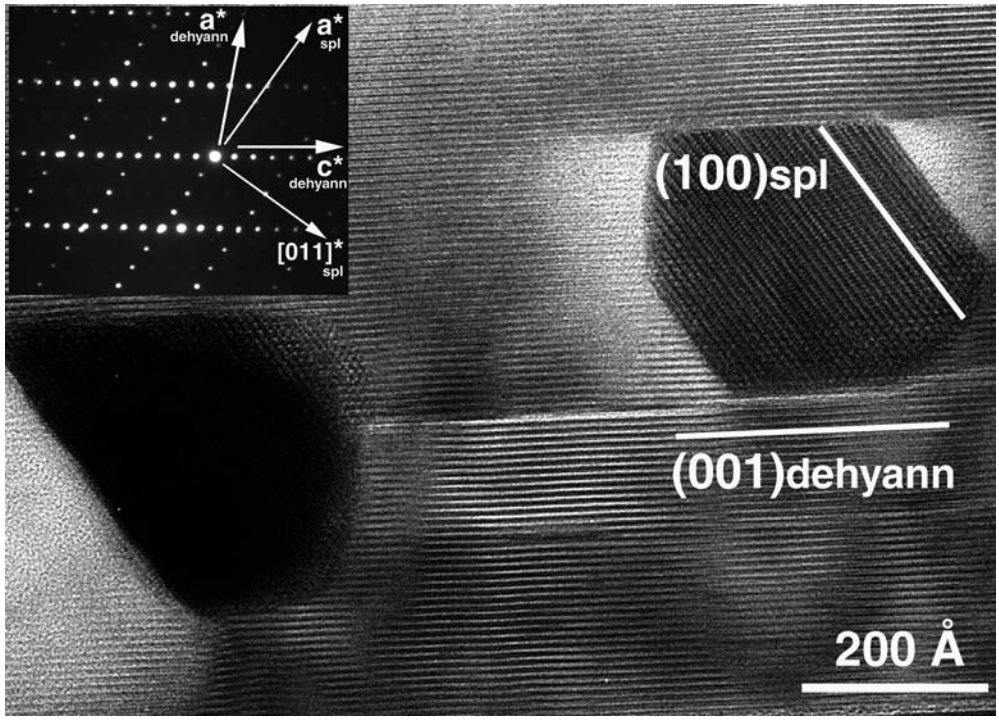

Fig. 3 Spinel inclusions (*dark grains*) within dehydrated annite: $(100)_{spl}$ lattice fringes form an angle of ~55 ° with $(001)_{dehyann}$. The *light contrast material* associated to spinel is silica glass. Inset $[0\bar{1}1]$ SAED pattern of spinel, overlapped to [010] pattern of dehydrated annite. $[111]^*_{spl}$ lies along $[001]^*_{dehyann}$

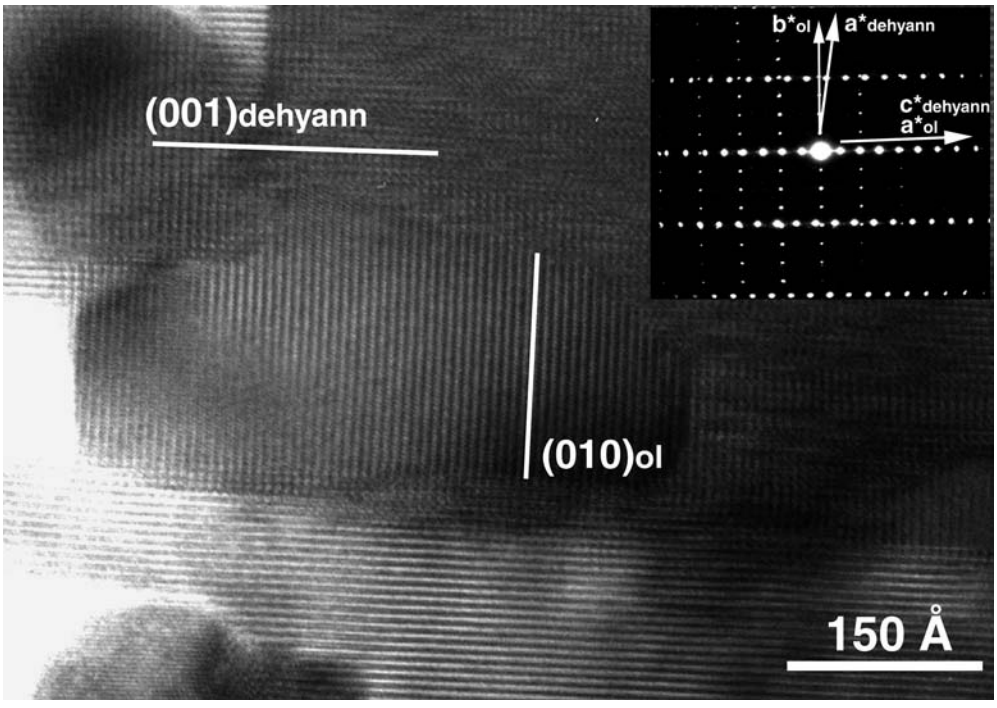

Fig. 4 inset [001] SAED pattern of olivine overlapped to [010] dehydrated annite. **a** Corresponding TEM image, with anhedral olivine within dehydrated annite. $(010)_{ol}$ are perpendicular to $(001)_{dehyann}$.

Spinels show ordered 8-Å (100) lattice fringes, forming an angle of ~55 ° with respect to $(001)_{dehyann}$ (Fig. 3). Spinels are often associated with glass (light contrast material). The outer shape of the spinel crystals may be limited by sharp crystallographic planes or by curved surfaces. Sharp planes correspond to dehydrated annite–spinel interfaces and to (100) spinel faces; otherwise, curved interfaces occur between spinel and silica glass.

Spinel composition is variable, with high Al and Fe contents and minor Mg and Ti. Table 2 reports the two extreme Al-richest and Fe-richest compositions. No Mg partitioning occurs; Ti preferentially enters the Fe-rich spinel. Al-rich spinels are more abundant than Fe-rich spinels. Elongated dark grains usually are Al-rich spinels, whereas equant dark grains are Fe-rich spinels.

2. Olivine occurs as anhedral grains, up to 2000 Å in size, and as smaller grains hosted within negative crystals together with silica glass (Figs. 4 and 5, respectively).

Olivine SAED patterns show sharp, intense reflections. In what follows, we refer to the olivine cell setting with lattice parameters $a = 4.82$ Å, $b = 10.48$ Å, $c = 6.08$ Å (values for pure fayalite). Both [001] and [010] SAED patterns were collected. Figure 4 (inset) reports overlapped $[001]_{ol}$ and $[010]_{dehyann}$ SAED patterns. The measured d_{100}, d_{010} and d_{001} of olivine are 4.80, 10.50 and 6.08 Å, respectively, namely larger than

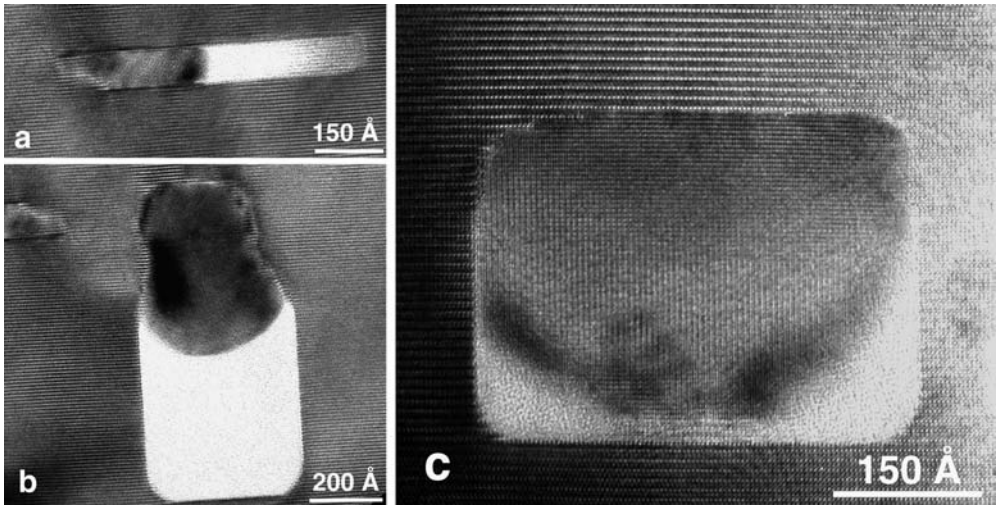

Fig. 5a–c HR images of olivine-bearing negative crystals, having different habits (elongated in a and **b**, equant in **c**). Olivine is seen along [010], whereas the host dehydrated annite is seen along [100]. In all images, $(001)_{dehyann}$ and $(100)_{ol}$ lattice fringes are horizontal

expected on the basis of TEM-EDS compositions (Table 2). We wonder whether these values may indicate strained parameters of olivine, similar to cryptoperthitic feldspars (e.g. Kroll and Ribbe 1983; Yund and Tullis 1983).

Olivine also shows constant crystallographic orientation with respect to dehydrated annite. In particular, b_{ol} is parallel to $a_{dehyann}$, c_{ol} to $b_{dehyann}$, whereas a_{ol} and $c_{dehyann}$ form an angle of $(\beta_{dehyann} - 90)°$. By comparison of the lattice parameters at the interface, we observe values larger for dehydrated annite than for olivine:

$a_{dehyann} \times 2 = 10.86\,\text{Å}$ vs. $b_{ol} = 10.50\,\text{Å}$
$b_{dehyann} = 9.33\,\text{Å}$ vs. $c_{ol} \times 1.5 = 9.12\,\text{Å}$
$c_{dehyann} = 10.25\,\text{Å} (d_{001} = 10.09)$ vs. $a_{ol} = 4.80 \times 2 = 9.60\,\text{Å}$.

Therefore, we note that the coherent olivine-dehydrated annite interfaces are associated to minor elastic strain, with strain energy roughly proportional to the lattice parameter ratios (1.03, 1.04 and 1.05, respectively).

Figure 4 shows an anhedral olivine grain, with rounded boundaries; $(010)_{ol}$ fringes are perpendicular to $(001)_{dehyann}$ and form regular sequences, without defects. The boundary between olivine and host-dehydrated annite is poorly defined, with local overlapping of lattice fringes (Moiré effects).

Figure 5a–c shows [010] high-resolution images of olivine grains, occurring within negative crystals together with glass (light contrast material). Host-dehydrated annite is seen along [100]. $(100)_{ol}$ lattice fringes are parallel to $(001)_{dehyann}$.

Negative crystals have variable habits, from equant to elongated, with elongation parallel (Fig. 5a) or orthogonal (Fig. 5b) with respect to $(001)_{dehyann}$. Note that different interfaces occur. They are sharp in the case of dehydrated annite – glass boundaries. They may be irregular and stepwise in the case of dehydrated annite – olivine boundaries, with possible layer-bending and dislocations close to the interface (Fig. 5b, upper part). Interfaces are always curved in the case of the olivine – glass boundaries, oriented either suborthogonal (Fig. 5a) or subparallel (Fig. 5b, c) with respect to $(001)_{dehyann}$.

Figure 6 shows an example of coherent boundary between olivine and dehydrated annite (Fourier-filtered HR image). $(001)_{dehyann}$ and $(010)_{dehyann}$ planes are coherent and continuous with respect to $(100)_{ol}$ and $(001)_{ol}$, respectively. Dehydrated annite and olivine are highly ordered, even close to the interface. No dislocations have been observed.

Olivine composition is constant (Table 2), with systematic deviation from the expected 2:1 stoichiometry. In fact, octahedral cations systematically sum up to 1.83 apfu. This feature may indicate partial occurrence of oxidized iron, namely of a lahiunitic component. In that case, the chemical formula of post-transformation olivine would be written $(Mg_{0.77}\ Fe^{2+}_{0.67}\ Fe^{3+}_{0.34}\ Mn_{0.05})_{\Sigma=1.83}Si_{1.00}\ O_{4.00}$. Finally, note that Mn from the originary chlorite is completely partitioned into olivine.

3. Glass typically occurs within negative crystals, together with spinels and olivine. It appears as a low-contrast material, associated to the dark crystalline grains. No diffraction effect occurs in the corresponding SAED pattern. Average composition (Table 2) indicates silicatic glass with variable Al content and minor Fe.

Sharp glass-dehydrated annite interfaces define the faces of the negative crystals. On the other hand, smoothed curved surfaces may occur when glass is in contact with olivine and spinel. These surfaces have a definite curvature polarity, with crystals systematically forming the convex side and glass forming the concave one.

IR and Raman spectra

Vibrational spectra allow identification of OH bonds, characterized by prominent stretching vibration frequencies in the 3000–4000-cm^{-1} range. Micro-IR and micro-Raman investigations were then carried out for the untreated sample and for the laser-heated samples, to characterize their water contents. Figure 7 reports the

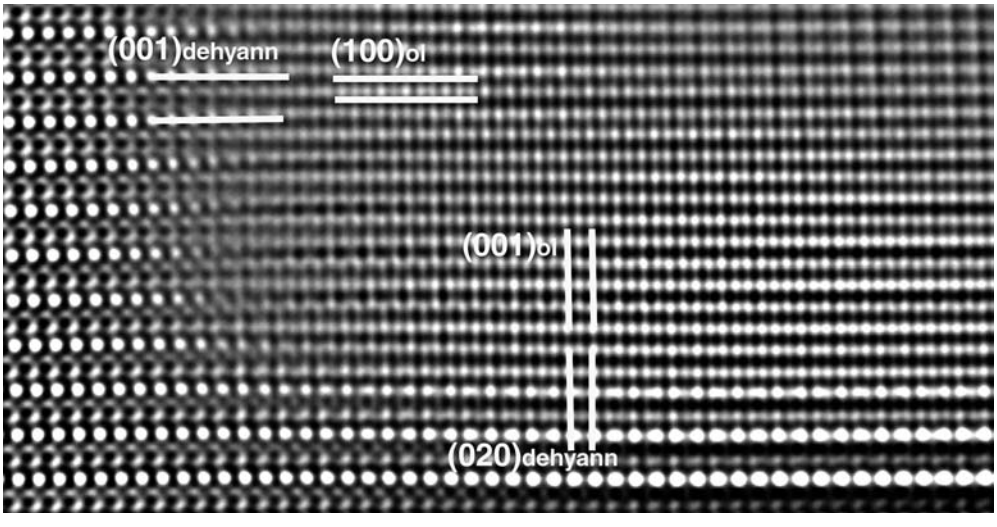

Fig. 6 Fourier-filtered TEM image, showing a coherent, defect-free interface between olivine (*upper right*) and dehydrated annite (*lower left*)

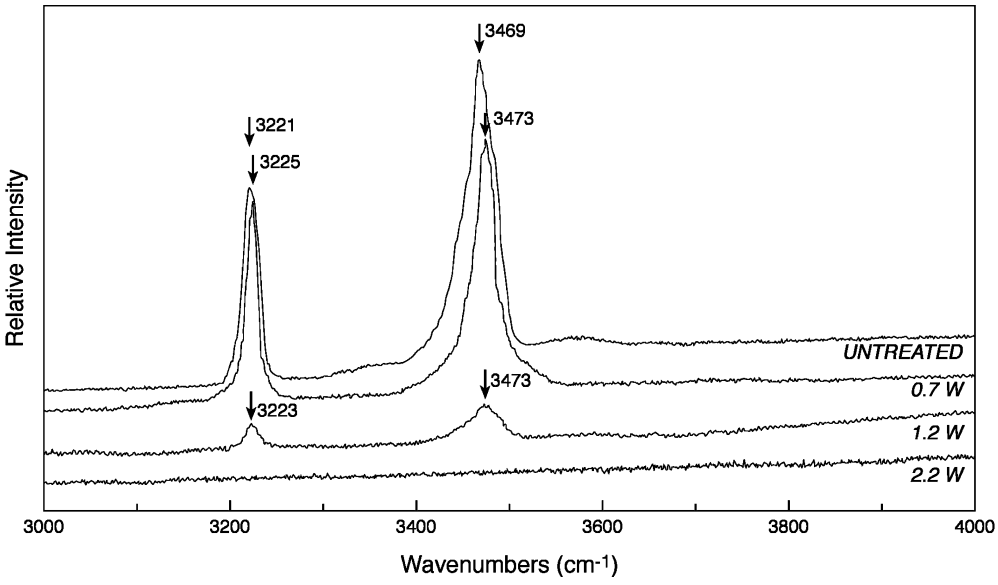

Fig. 7 Micro-Raman spectra of the untreated, 0.7-,1.2- and 2.2-W samples

micro-Raman spectra (3000–4000 cm^{-1}) for the untreated sample and for samples heated at 0.7, 1.2 and 2.2 W, respectively. The spectra reveal vanishing OH signals with increasing laser power, thus indicating the progressive dehydration of annite and chamosite. OH signals completely disappear in the 2.2-W sample.

Similarly, IR spectra of untreated samples show evident OH-stretching vibrations (in particular, broad IR peaks close to 3600 cm^{-1} with shoulders towards low wavenumbers). These signals completely disappear in the 2.2-W sample, thus confirming its anhydrous nature.

Therefore, based upon electron diffraction, TEM-EDS analyses, IR and Raman indications, we conclude that, after laser heating, we are actually dealing with dehydrated annite.

Thermal analyses

Thermal analyses have been carried out up to 1200 °C on the untreated chloritized annite (no. AR8) and on a chlorite-free annite (no. A13, described in Di Vincenzo et al. 2003).

TG: Most of the weight loss occurs between 450 and 650 °C, with total loss of 1.86 and 6.12 wt% for A13 and AR8, respectively (Fig. 8a). As the theoretical water content of A13 is close to 3.7 wt%, we conclude that volatiles are released as a mixture of 45% H_2O and 55% H_2. This is equivalent to state that 1.1 iron apfu are oxidized, with weight gain close to 1.9 wt%.

In the case of AR8, the 6.12 wt% weight loss would correspond to 34% chlorite. However, due to partial iron oxidation, this represents a lower estimate of the actual volume, that should be closer to 43%, as indicated by X-ray diffraction.

DTG: AR8 shows a broad peak at 83 °C (loss rate of 18.6 $\mu g\ min^{-1}$), due to adsorbed water (Fig. 8b). The curve is characterized by a sharp peak at 531 °C (77.1 $\mu g\ min^{-1}$). Mass spectra reveal ions with 17, 18 and 19 amu (atomic mass unit), respectively, corresponding to OH, H_2O and H_3O^+. At higher temperature (716 °C, $-3.4\ \mu g\ min^{-1}$), the curve shows a slight weight gain.

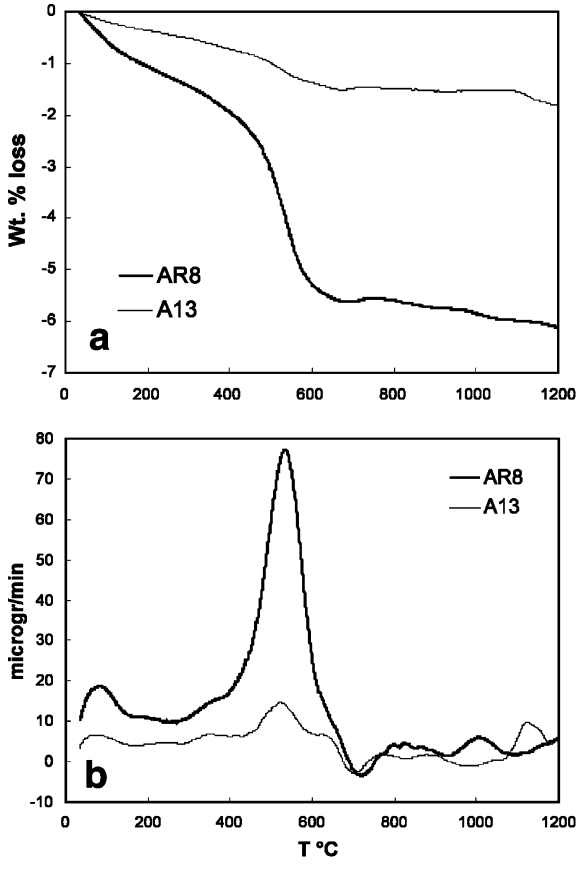

Fig. 8a TG curves of chloritized annite (AR8, our sample) and, for comparison, of chlorite-free annite (A13). **b** DTG curves for AR8 and A13

A13 shows a weak signal at 71 °C (6.6 μg min^{-1}), from adsorbed water. Dehydration peak occurs at 524 °C, similar to chloritized annite (AR8). Mass spectra for OH, H_2O and H_3O^+ have been observed, thus confirming that the weight loss corresponds at least in part to water loss, even for chlorite-free biotite. The 524 °C peak is weaker, with lower weight loss rate (14.7 μg min^{-1} vs. 77.1 μg min^{-1}). Slight weight gain is evident at high temperature (797 °C, -2.9 μg min^{-1}).

XRPD patterns of heated powders reveal hematite and maghemite as the only crystalline phases occurring at 1200 °C, in both AR8 and A13 samples.

Discussion

Microstructural evidence, spectroscopic and thermal analyses

0.3-W (600 °C) sample

TEM shows a poorly crystalline sample, with evidence for chlorite breakdown and annite dehydration. This agrees with thermal analyses, showing important water release between 450 and 650 °C. In particular, TG and DTG curves show chlorite and mica dehydrations in the same temperature range, with overlapped processes. IR and Raman spectra still show OH signals, with intensity lower than in the untreated sample.

Weight loss requires negative volume variation. This negative variation determines frequent interlayer parting in mica.

Intermediate samples: 0.7 W (810 °C) and 1.2 W (940 °C)

Samples 0.7 W and 1.2 W are poorly crystalline, with dehydrated annite showing incipient structural reorganization. Chlorite is completely absent and its breakdown products start to crystallize.

Weight loss at temperature higher than 800 °C is low, thus suggesting almost anhydrous sample. However, the Raman spectrum of sample 0.7 W still reveals OH signals.

2.2-W (1080 °C) sample

Laser heating up to 1080 °C produces crystalline, annealed dehydrated annite. The sample is completely anhydrous, as indicated by both thermal analyses and spectroscopic investigations. Basal spacing of dehydrated annite is slightly lower than for the untreated annite. Variant orientations for dehydrated annite (namely, a^*c^* and b^*c^* orientations) indicate major reorganization within mica, involving nucleation and growth processes.

TEM showed no evidence for dehydrated annite breakdown. Conversely, XRPD pattern of the TG-DTA heated sample (1200 °C) revealed only maghemite and magnetite. We interpret these data as suggesting final breakdown of dehydrated annite in the temperature range 1080–1200 °C, producing Fe oxides plus silica melt. Mass balance requires that the specimen should finally consist of 10% maghemite, 35% spinels, 15% olivine and 40% silica and potassium glass. Notwithstanding the several checks, we were unable to find any trace for olivine in the final XRPD. This may be tentatively explained by masking effects from glass and oxides, or by a further final olivine oxidation at temperature close to 1200 °C.

Thermal breakdown of chlorite

Brindley and Ali (1950) studied thermal transformation in magnesian chlorite, observing two dehydration stages. Close to 600 °C, chlorite loses 50% water, but keeps the main features of chlorite, transforming to the so-called modified chlorite (MC; Bai et al. 1993; Zhan and Guggenheim 1995). This dehydration occurs in the brucite sheet and the resulting MC has a shrinked c periodicity (e.g. 14.45 to 14.09 Å; Brindley and Ali 1950). MC is stable and remains unchanged even after immersion in water for several weeks. In the second dehydration stage, close to 800 °C, newly formed olivine is produced. Spinel and probably enstatite appear at higher temperatures.

Fawcett and Yoder (1966) found that chlorite decomposes to forsterite + cordierite + spinel + vapour below 3.5 kbar, and to forsterite + enstatite + spinel + vapour above 3.5 kbar, at temperatures close to 770 °C. Cho and Fawcett (1986) studied the chlorite breakdown to forsterite + cordierite + spinel + vapour, proposing transformations through reaction intermediates such as 7 Å-chlorite and fine-grained amorphous oxide mixtures.

However, our fast experiments do not result in the stable low-pressure phase assemblage (forsterite + cordierite + spinel + vapour). Although we observe forsterite + spinel, cordierite is replaced by silica-rich glass. Based upon the average TEM-EDS compositions, dehydration of our chamosite obeys the reaction:

$$\begin{aligned}&\text{chamosite } (Mg_{1.13}Fe_{3.25}Al_{1.49}Mn_{0.07}Ti_{0.06})_{\Sigma=6.00}\\&(Si_{3.25}Al_{0.74})_{\Sigma=4.00}O_{10.82}(OH)_{7.18} >\\&\quad > \text{olivine } (Mg_{0.77}Fe^{2+}_{0.67}Fe^{3+}_{0.34}Mn_{0.05})_{\Sigma=1.83}Si_{1.00}O_{4.00}+\\&\quad + \text{spinel } (Mg_{0.16}Fe^{2+}_{0.65}Fe^{3+}_{0.83}Al_{1.19}Ti_{0.17})_{\Sigma=3.00}O_{4.00}+\\&\quad + \text{Si-glass } (Fe_{0.07}Al_{0.25}Si_{0.68})_{\Sigma=1.00}O_{1.80}\\&\quad + \text{vapour.}\end{aligned}$$

Mass balance requires that chlorite decomposes to 39% olivine, 27% Si glass, 20% Al spinel and 14% Fe spinel. These nanochemical expectations are largely in

agreement with the nanotextural TEM observations. Thermal breakdown products differ strongly in chemical composition, magnesium being strongly partitioned to olivine, iron and aluminum to spinel, silicon to glass.

The annite thermal transformation

After heating in the 450–650 °C range, annite transforms to dehydrated products, as indicated by Raman and IR spectral evidence (OH signals disappearing with increasing temperature).

Thermal analyses suggest weight loss lower than the expected water content of annite, due to partial iron oxidation. As the simultaneous mass spectra indicate water within the thermally released volatiles, we conclude that volatiles are released as a mixture formed by 45% H_2O and 55% H_2.

The previous features are important to understand the nature of thermally transformed annite with respect to two possible different models. Annite might transform to oxyannite, by hydrogen loss coupled with iron oxidation. The idealized reaction would be:

$$K\,Fe^{2+}{}_3Al\,Si_3\,O_{10}(OH)_2 \rightarrow K\,Fe^{2+}\,Fe^{3+}{}_2Al\,Si_3O_{12} + H_2,$$

as suggested by the experiments of Wones and Eugster (1965) or Ferrow (1987). Alternatively, annite may transform to dehydroxylated annite, by condensation of two hydroxyls and water loss. The idealized reaction would be

$$K\,Fe^{2+}{}_3Al\,Si_3\,O_{10}(OH)_2 \rightarrow K\,Fe^{2+}{}_3Al\,Si_3\,O_{11} + H_2O,$$

as suggested by Vedder and Wilkins (1969) or Sanz et al. (1983). The most important differences between the two models are presence of Fe^{3+} and absence of vacancies in oxyannite, and presence of Fe^{2+} coupled with anionic vacancy in dehydroxylated annite.

Our spectroscopic and thermal data indicate that annite may undergo both processes, partially transforming to oxyannite and to dehydroxylated annite. In the latter case, the mechanism would not be too different from that described in Mazzucato et al. (1999) for muscovite (that is " a dehydroxylation process, involving the nucleation and growth of the high temperature dehydroxylated phase, having Al in fivefold coordination"), with the obvious difference of having $^{V}Fe^{2+}$ rather than $^{V}Al^{3+}$.

Negative crystals and topotactic relationships

In the 2.2 W section above, we have shown that olivine and spinels, formed after chlorite breakdown, are hosted within euhedral negative crystals and exhibit strict crystallographic relationships with the host-dehydrated annite.

The overall texture of the 2.2-W sample results from a complex thermal transformation, consisting of two main steps. At lower temperature, we observe decreasing annite crystallinity and chlorite breakdown, with production of amorphous layers roughly parallel to the originaly $(001)_{chl}$. At higher temperature, the sample undergoes annealing, with important cation diffusion and structural reorganization. In particular, amorphous (001) packets coalesce to form equant, rounded inclusions that further evolve to euhedral negative crystals and undergo crystallization (olivine and spinels), leaving a silica-rich glass residual.

At the same time, dehydrated annite becomes highly crystalline and assumes topotactic relationships with respect to included olivine and spinels.

The topotactic relationships among dehydrated annite, spinels and olivine are explained on the basis of the existence of tight nucleation and growth paths, capable of controlling the orientation of the new phases. In particular, these geometrical relationships may be explained assuming that, during thermal transformation, the oxygen framework is conserved (i.e. oxygens do not move) while cations diffuse through the framework. In other words, we may consider the different structures as built by hexagonally close-packed oxygen layers that conserve their stacking sequences all along the different thermal transformations. Inspection of the structures reveals that these hexagonally close-packed oxygen layers lay along $(001)_{dehyann}$, $(001)_{chl}$, $(100)_{ol}$ and $(111)_{spl}$. Therefore, these elements are parallel after thermal transformation.

As previously stated, the olivine-dehydrated annite boundary is associated with elastic strain, with strain energy roughly proportional to the lattice parameter ratios. In the case of the $(100)_{ol}$ / $(001)_{dehyann}$ boundary, no further misfit occurs, thus appearing as coherent or semicoherent boundary in the electron microscopy images. Conversely, the $(001)_{ol}$ / $(010)_{dehyann}$ boundary is associated with greater strain energy, resulting from the lack of coincidence of the $c_{dehyann}$ and the a_{ol} directions (namely, whereas the hexagonally close-packed oxygen layers overlap following the orthogonal idealized AB sequence in olivine, these layers do not overlap along an orthogonal direction in mica, due to the interposition of interlayer cations). This higher strain energy reduces the interface coherency and produces strain features in the electron image contrast.

Conclusions

During laser-heating, chloritized annite continuously undergoes major structural reorganization. Chlorite breaks down and recrystallizes as olivine and spinels, hosted within negative crystals together with silica glass.

Negative crystals are embedded within a new matrix, consisting of ordered dehydrated annite. Olivine, spinels and dehydrated annite are topotactically oriented and share hexagonally close-packed oxygen layers.

Acknowledgements We are indebted to D. Malferrari (University of Modena) and to P. Marianelli (University of Pisa), for providing thermal and infrared analyses, respectively.

References

Bai T, Guggenheim S, Wang S, Rancourt DG, Koster Van Groos AF (1993) Metastable phase relations in the chlorite–H_2O system. Am Mineral 78: 1208–1216

Brindley GW, Ali SA (1950) X-ray study of thermal transformations in some magnesian chlorite minerals. Acta Crystallogr 3: 25–30

Cliff G, Lorimer GW (1975) The quantitative analysis of thin specimens. J Microscr 103: 203–207

Cho M, Fawcett JJ (1986) A kinetic study of clinochlore and its high temperature equivalent forsterite–cordierite–spinel at 2 kbar water pressure. Am Mineral 71: 68–77

Di Vincenzo G, Viti C, Rocchi S (2003) The effect of chlorite interlayering on ^{40}Ar–^{39}Ar biotite dating: an ^{40}Ar–^{39}Ar laser probe and TEM investigation of variably chloritised biotites. Contrib Mineral Petrol 145: 643–658

Fawcett JJ, Yoder HS (1966) Phase relationships of chlorites in the system MgO–Al_2O_3–SiO_2–H_2O. Am Mineral 51: 353–380

Ferrow E (1987) Mossbauer and X-ray studies on the oxidation of annite and ferriannite. Phys Chem Miner 14: 270–275

Kroll H, Ribbe PH (1983) Lattice parameters, composition and Al, Si order in alkali feldspars. In Ribbe PH. (ed), Feldspar mineralogy, Reviews in Mineralogy, vol 2 Minerlogical Society America, Washington DC pp 57–100

Maniar PD, Cooke GA (1997) Modal analyses of granitoids by quantitative X-ray diffraction. Am Mineral 72: 433–439

Mazzucato E, Artioli G, Gualtieri A (1999) High-temperature dehydroxylation of muscovite $2M_1$: a kinetic study by in situ XRPD. Phys Chem Miner 26: 375–381

Mellini M, Menichini R (1985) Proportionality factors for thin film TEM/EDS microanalysis of silicate minerals. Rend Soc Ital Mineral Petrol 40: 261–266

Sanz J, Gonzales-Carreno T, Gancedo R (1983) On dehydroxylation mechanism of a biotite in vacuo and in oxygen. Phys Chem Miner 9: 14–18

Vedder W, Wilkins WT (1969) Dehydroxylation and rehydroxylation, oxidation and reduction of micas. Am Mineral 54: 482–509

Viti C, Frezzotti ML (2001) Transmission electron microscopy applied to fluid inclusion investigations. Lithos 55: 125–138

Wones DR, Eugster HP (1965) Stability of biotite: experiment, theory and application. Am Mineral 50: 1228–1272

Yund RA, Tullis J (1983) Subsolidus phase relations in the alkali feldspars with emphasis on coherent phases. In Ribbe PH. (ed) Feldspar mineralogy, Reviews in Mineralogy, vol. 2 Minerlogical Society America, Washington DC pp 141–176

Zhan W, Guggenheim S (1995) The dehydroxylation of chlorite and the formation of topotactic product phases. Clays Clay Miner 43: 622–629